Available online at www.sciencedirect.com
ScienceDirect
Computers & Fluids 35 (2006) 1193–1204
computers & fluids
www.elsevier.com/locate/compfluid

The method of boundary condition transfer in application to modeling near-wall turbulent flows

S.V. Utyuzhnikov *

Department of Power, Propulsion & Aerospace Engineering, School of Engineering, Cranfield University, Cranfield MK43 0AL, UK

Received 15 August 2004; received in revised form 1 March 2005; accepted 31 May 2005
Available online 26 September 2005

Abstract

Generalized wall functions in application to high-Reynolds-number turbulence models are derived. The wall functions are based on transfer of a boundary condition from a wall to some intermediate boundary near the wall (usually the first nearest to the wall mesh point but that is not obligatory). The boundary conditions on the intermediate boundary are of Robin-type and represented in a differential form. The wall functions are obtained in an analytical easy-to-implement form, can take into account source terms such as pressure gradient and buoyancy forces, and do not include free parameters. The log-profile assumption is not used in this approach. Both Dirichlet and Newman boundary-value problems are considered. A method for complementing solution near the wall is suggested. Although the generalized wall functions are obtained for the k–ϵ model, generalization to other turbulence models is straightforward. The general approach suggested is applicable to studying high-temperature regimes with variable laminar viscosity and density. A robust numerical algorithm is proposed for implementation of Robin-type wall functions. Test results made for a channel flow and axisymmetric impinging jet have showed reasonably good accuracy, reached without any case-dependent turning, and a weak dependence of the solution on the location of the intermediate boundary where the boundary conditions are set. It is demonstrated that the method of boundary condition transfer applied to low-Reynolds-number turbulence models can be used as a decomposition method.
© 2005 Elsevier Ltd. All rights reserved.

1. Introduction

The problem of mathematical simulation of turbulent flows near walls appears in many practical applications. It is well known that turbulence vanishes near a wall due to the no-slip boundary condition for the velocity as well as the blocking effect caused by the wall. In the vicinity of the wall, there is a thin sublayer with predominantly molecular diffusion and viscous dissipation. The sublayer has a substantial influence upon the remaining part of the flow. An adequate numerical resolution of a solution in the sublayer requires a very fine mesh because of the thinness of the sublayer and high gradients of the solution. It makes a model used time consuming and often not suitable for industrial applications. Because of the low turbulent Reynolds number in the sublayer, models that resolve the sublayer are called low-Reynolds-number (LR) models.

So-called high-Reynolds-number (HR) models do not provide resolution of the viscous sublayer. In this type of models the sublayer domain is not directly resolved. It significantly saves computational efforts [1]. In the HR models, the boundary conditions or near-wall profiles are represented by wall functions. In most cases, the wall functions are semi-empirical and have very limited applications [1–3,7,8]. First wall functions are based on the log-law profile assumption for the velocity [7,8]. Thus, they are only applicable to very simple near-wall flows. The main disadvantage of these wall functions is a strong dependence on the location of the mesh point

* Tel.: +44 161 306 37 07; fax: +44 161 306 37 23.
E-mail addresses: s.v.utyuzhnikov@cranfield.ac.uk, s.utyuzhnikov@manchester.ac.uk

0045-7930/$ - see front matter © 2005 Elsevier Ltd. All rights reserved.
doi:10.1016/j.compfluid.2005.05.005

closest to the wall where the wall functions are applied. Such a problem is especially pronounced if the first mesh point is located inside the viscous sublayer. To avoid this, the scalable wall function approach is suggested in [9,10]. Wilcox showed [11] that pressure gradient must be taken into account to avoid the mesh dependence. In more recent approaches [1–3] attempts have been made to take into account the pressure gradient and other effects such as buoyancy forces. Numerical comparisons done in [1–3] showed that such advanced wall functions give substantially better prediction than the standard wall functions. A brief review of wall functions can be found in, e.g., [1,2]. Sub-grid numerical wall functions are developed in [2,4] where dependent variables are determined by solving boundary-layer-type transport equations in a near-wall sub-grid. In this approach, the boundary condition on the boundary that is opposite to the wall is determined by linear interpolation of certain main-grid values. In [3], analytical wall functions are obtained by integrating boundary-layer-type equations in the wall vicinity using the assumption that all terms besides the diffusive one are constant. Mainly, it means that the contribution of the convective terms is neglected near the wall and the pressure gradient and buoyancy force (if applicable) are not changed. At the wall, the boundary conditions are the same as those used in the LR models. An analytical profile for the turbulent viscosity are then used in the cell nearest to the wall to reconstruct the near-wall solution. The wall functions for the turbulent kinetic energy and its dissipation are based on the local analytical solution for the velocity in the near-wall cell. Although approaches [1–3] allow one to make substantially better prediction in comparison to the standard methods, the realization of them is quite complicated especially in the case of their implementation into industrial codes. The wall functions [1–4] can be represented in a finite-difference form only. Although this form is suitable for finite-volume algorithms, its use for finite-difference approximations is not clear. Similar to the standard wall functions, this approach faces substantial problems if the nearest to the wall cell is in the viscous sublayer. To resolve this problem, an empirical correlation function is introduced for dissipation rate [3] that allows one to take into account a laminarization effect. Also, it is important to note that the second to the wall cell cannot be much smaller or bigger than the first one because of the integration over the first cell.

In the following sections, the method of boundary condition transfer is used [12]. The method allows us to transfer a boundary condition from the wall to some intermediate surface. It is shown that it is possible to transfer the boundary condition either approximately (analytically) or exactly (numerically). The boundary conditions on the intermediate surface are always of Robin-type (or mixed) and represented in a differential form. They can take into account the influence of the source terms in governing equations. These boundary conditions are interpreted as generalized (Robin-type) wall functions. The location of the point, to which the boundary conditions are transferred, does not make any considerable effect on the mesh distribution nearby this point. The wall functions can be easily used especially in finite-difference approximations. A method for complementing the solution on the entire domain outside the viscous sublayer is suggested. It is worth noting that at the time being Robin-type (mixed) boundary conditions are not widely used in turbulence modeling community. At the same time, they are extensively employed in other fields of fluid mechanics, e.g., dynamics of rarefied gas and radiation.

Numerical intermediate Robin-type boundary conditions are developed along with a decomposition method. The method allows us to split the boundary-value problem into two parts: an inner problem (in the region nearest to the wall) and an outer problem (in the rest region). Both boundary-value problems can be solved independently, using different numerical schemes and meshes, which yields the terminal solution. The inner solution can be then used for complementing the solution near the wall if HR models are applied along with the generalized wall functions.

The general approach suggested is applicable to studying high-temperature turbulent flows with variable density and laminar viscosity. It can be also applied for the development of the appropriate boundary conditions for the Reynolds Averaged Navier–Stokes equations (RANS) and large eddy simulation (LES). In the latter case, it can be especially effective in conjunction with the monotone integrated approach (MILES) [13] based on high-resolution approximations to provide consistent approximation in near-wall turbulent flow modeling.

2. Model equation

First, let us consider the following model equation:

$$(\mu u_y)_y = R_h \tag{1}$$

defined in a domain $\Omega = [0, y_e]$ with Dirichlet boundary conditions:

$$u(0) = u_0, \quad u(y_e) = u_1. \tag{2}$$

Eq. (1) represents the general form of the boundary-layer-type equation. The right-hand side R_h is an appropriate source term including, e.g., the pressure gradient in the momentum equation.

Assuming that $R_h = \text{const}$, after integrating Eq. (1) from 0 to y, one obtains:

$$\tau_w = \mu(y)\mathrm{d}u/\mathrm{d}y(y) - R_h y, \tag{3}$$

where $\tau_w = \mu(y)\mathrm{d}u/\mathrm{d}y(y)_w$. Index w here and below means a value at $y = 0$. The second integration gives

$$u(y) = u_0 + \tau_w \int_0^y \frac{\mathrm{d}\xi}{\mu} + R_h \int_0^y \frac{\xi}{\mu}\mathrm{d}\xi. \tag{4}$$

Considering (3) and (4) at some intermediate point y^* in Ω and replacing τ_w, we have

$$u(y^*) = u_0 + f_1 \frac{\mathrm{d}u}{\mathrm{d}y}(y^*) - \frac{R_h}{\mu(y^*)} f_2, \tag{5}$$

where

$$f_1 = \int_0^{y^*} \frac{\mu(y^*)}{\mu(y)}\mathrm{d}y, \quad f_2 = \int_0^{y^*} \frac{\mu(y^*)}{\mu(y)}(y^* - y)\mathrm{d}y. \tag{6}$$

Relation (5) can be interpreted as a Robin-type boundary condition transferred from a wall ($y = 0$) to some point y^* inside the domain Ω. This boundary condition can be either exact (if the exact function of μ is used in (6)) or approximate (if μ is estimated by one way or another).

If $R_h = R_h(y)$, then

$$u(y^*) = u_0 + f_1 \frac{\mathrm{d}u}{\mathrm{d}y}(y^*) - \left(\int_0^{y^*} R_h\,\mathrm{d}y\right)\frac{f_2}{y^*\mu(y^*)}, \tag{7}$$

where

$$f_1 = \int_0^{y^*} \frac{\mu(y^*)}{\mu(y)}\mathrm{d}y,$$
$$f_2 = y^* \int_0^{y^*} \frac{\mu(y^*)}{\mu(y)}\left(1 - \frac{\int_0^y R_h\,\mathrm{d}y}{\int_0^{y^*} R_h\,\mathrm{d}y}\right)\mathrm{d}y. \tag{8}$$

Assuming that the coefficient varies piece-wise linearly

$$\mu = \begin{cases} \mu_w, & \text{if } 0 \leqslant y \leqslant y_v, \\ \mu_w + (\mu^* - \mu_w)\frac{y - y_v}{y^* - y_v}, & \text{if } y_v \leqslant y \leqslant y^*, \end{cases}$$

it is possible to obtain analytical expressions for f_1 and f_2 if $R_h = \text{const}$ and $y_v \leqslant y^*$:

$$f_1 = \alpha_\mu y_v(1 + \theta \ln \alpha_\mu),$$
$$f_2 = \alpha_\mu y_v[(1 - \theta)y^* + y_v(\theta^2 \alpha_\mu \ln \alpha_\mu - 1/2 + \theta)], \tag{9}$$

where $\alpha_\mu = \mu^*/\mu_w, \theta^{-1} = \frac{\mu^* - \mu_w}{\mu_w}\frac{y_v}{y^* - y_v}$. The parameter θ represents cotangent of the inclination angle of the dependence μ/μ_w on y/y_v.

The coefficient μ_w is assumed to be constant. In a more general case, it is not difficult to take into account a possible variation of the coefficient μ_w in the interval $[0, y_v]$ as in [3].

Upon solving the problem with boundary condition (5), the wall-flux τ_w can be found from (5) and (3) written at y^* as follows:

$$\tau_w = \frac{\mu^* u(y^*)}{f_1} + (f_2/f_1 - y^*)R_h. \tag{10}$$

This formula can be easily generalized on the case of a variable right-hand side R_h using (7).

Once a Newmann problem is solved:

$$\mathrm{d}u/\mathrm{d}y(0) = \tau_w/\mu_w, \quad u(y_e) = u_1, \tag{11}$$

the intermediate boundary condition at $y = y^*$ is simpler than in the previous case:

$$\frac{\mathrm{d}u}{\mathrm{d}y}(y^*) = \left(\tau_w + \int_0^{y^*} R_h\,\mathrm{d}y\right)\Big/\mu^*, \tag{12}$$

The boundary conditions are always linear if governing equation (1) is linear. They are represented in a differential–integral form which can be easy realized especially with finite-difference approximations. It is easy to see that mesh distribution possible in the interval $[y^*, y_e]$ can be independent on the location of the intermediate boundary corresponding to the point y^*.

In application to the Reynolds averaged Navier–Stokes equations (RANS), the method of boundary condition transfer considered here gives generalized Robin-type wall functions.

3. Generalized (Robin-type) wall functions

We apply the method of boundary condition transfer given above to derive the generalized wall functions for the tangential and normal velocity components U and V, temperature T, and turbulent kinetic energy k.

Neglecting diffusion parallel to the wall, the momentum and enthalpy transport equations can be written in the Cartesian coordinate system (x, y) as follows:

$$\frac{\partial}{\partial y}\left[(\mu_l + \mu_t)\frac{\partial U}{\partial y}\right] = \rho U\frac{\partial U}{\partial x} + \rho V\frac{\partial U}{\partial y} + \frac{\partial P}{\partial x}, \tag{13}$$

$$\frac{\partial}{\partial y}\left[(\mu_l + \mu_t)\frac{\partial V}{\partial y}\right] = \rho U\frac{\partial V}{\partial x} + \rho V\frac{\partial V}{\partial y} + \frac{\partial P}{\partial y}, \tag{14}$$

$$\frac{\partial}{\partial y}\left[\left(\frac{\mu_l}{Pr} + \frac{\mu_t}{Pr_t}\right)\frac{\partial T}{\partial y}\right] = \rho U\frac{\partial T}{\partial x} + \rho V\frac{\partial T}{\partial y}. \tag{15}$$

Here μ_l and μ_t are the laminar and turbulent viscosities, accordingly; Pr and Pr_t are Prandtl numbers; U and V are the velocity component in the (x, y) coordinate system; ρ is the density; P is the pressure.

It is easy to see that the equations have the same form as model equation (1).

Then, the intermediate boundary conditions for U, V and T at point y^* are given by (7) upon substitution U, V or T instead of u accordingly. Evidently, the coefficient μ must be considered as either $\mu_l + \mu_t$ or $\mu_l/Pr + \mu_t/Pr_t$. In the case of the momentum equation $u_0 = 0$. If y^* is chosen in the wall vicinity, the right-hand side R_h can be represented by a constant evaluating the terms at y^*. Thus, in the case of the momentum equations and enthalpy the relative right-hand sides are as follows:

$$R_h = R_{hu} \equiv \rho\left(U\frac{\partial U}{\partial x}(y^*) + V\frac{\partial U}{\partial y}(y^*)\right) + \frac{\partial P}{\partial x}(y^*), \quad (16)$$

$$R_h = R_{hv} \equiv \rho\left(U\frac{\partial V}{\partial x}(y^*) + V\frac{\partial V}{\partial y}(y^*)\right) + \frac{\partial P}{\partial y}(y^*), \quad (17)$$

$$R_h = R_{ht} \equiv \rho\left(U\frac{\partial T}{\partial x}(y^*) + V\frac{\partial T}{\partial y}(y^*)\right). \quad (18)$$

Thus, all the terms of the parabolized (reduced) Navier–Stokes equations (PNS) [14] are taken into account. Unlike [3], a similar approach is applied to the equation for the turbulence kinetic energy as well:

$$\frac{\partial}{\partial y}\left[\left(\mu_l + \frac{\mu_t}{Pr_k}\right)\frac{\partial k}{\partial y}\right] = \rho U\frac{\partial k}{\partial x} + \rho V\frac{\partial k}{\partial y} - P_k + \rho\epsilon, \quad (19)$$

where P_k is the production of the turbulent kinetic energy, ϵ is its dissipation; Pr_k is the Prandtl number.

Evaluating the convective terms, one obtains the following expression for right-hand side R_h:

$$R_h = R_{hk} \equiv \rho\left(U\frac{\mathrm{d}k}{\mathrm{d}x}(y^*) + V\frac{\mathrm{d}k}{\mathrm{d}y}(y^*)\right) + \rho\epsilon - \mu_t\left(\frac{\mathrm{d}U}{\mathrm{d}y}\right)^2. \quad (20)$$

Let us assume a piece-wise linear behavior of the function μ_t:

$$\mu_t = \begin{cases} 0, & \text{if } 0 \leqslant y \leqslant y_v, \\ \mu_t^* \frac{y - y_v}{y^* - y_v}, & \text{if } y_v \leqslant y \leqslant y^*, \end{cases} \quad (21)$$

where y_v is the thickness of the viscous sublayer near the wall. Then, the coefficients f_1 and f_2 in (8) (the latter term only if $R_h = \text{const}$) can be evaluated by (9).

For the momentum equation

$$\alpha_\mu = \mu^*/\mu_l, \quad \theta = \frac{y^* - y_v}{y_v}\frac{\mu_l}{\mu_t^*}, \quad \mu^* = \mu_l + \mu_t^*, \quad (22)$$

while in the case of the energy equation

$$\alpha_\mu = \frac{\mu_l/Pr + \mu_t^*/Pr_t}{\mu_l/Pr}, \quad \theta = \frac{y^* - y_v}{y_v}\frac{Pr_t}{Pr}\frac{\mu_l}{\mu_t^*}. \quad (23)$$

If the turbulent viscosity μ_t^* in (21) is evaluated as follows [3]:

$$\mu_t^* = C_\mu C_l \rho\frac{\sqrt{k^*}}{\mu_l} y_v \frac{y^* - y_v}{y_v}\mu_l = C_\mu C_l Re_v \frac{y^* - y_v}{y_v}\mu_l \approx 2.5\frac{y^* - y_v}{y_v}\mu_l, \quad (24)$$

where $k^* = k(y^*), C = 0.09, C_l = 2.55, Re_v \equiv \frac{\rho\sqrt{k^*}y_v}{\mu_l} = 10.8$, then θ is a constant equaled to 0.4 for the momentum equation.

It has been found from the computations that it is more accurate to evaluate the turbulent viscosity at y^* from the HR k–ϵ model directly

$$\mu_t = C_\mu\rho(k^*))^2/\epsilon \quad (25)$$

rather than from Eq. (24).

The sublayer thickness y_v is evaluated as follows [3]:

$$y_v = Re_v\mu_l/(\rho\sqrt{k_v}), \quad (26)$$

where k_v is the value of k at the edge of the viscous sublayer.

If $y^* < y_v$ then the boundary conditions are set inside the sublayer, and formulas (9) are not formally valid. The consideration of the boundary conditions (7) and (8) inside the sublayer is not fully appropriate because the model does not adequately take into account the blocking wall effects which are very important here. It is suggested to pose the boundary conditions at the edge of the sublayer $y = y_v$ as in [9] because y_v is small enough. Then, the coefficients f_1 and f_2 in (7) can be evaluated as follows:

$$f_1 = \alpha_\mu y_v, \quad f_2 = \alpha_\mu y_v^2/2. \quad (27)$$

It is assumed that the turbulent viscosity μ_t reaches value (25) at the edge of the viscous sublayer immediately. These boundary conditions are consistent with boundary conditions (9) taking in the limit $y^* \to y_v$ or $\theta \to 0$.

To evaluate $\epsilon(y)$, it is supposed that, as in [3], in the vicinity of a wall $\epsilon(y)$ is a continuous function which is constant in the wall vicinity and have an inverse dependence on y further. It gives the following approximation for $\epsilon(y)$:

$$\epsilon(y) = \begin{cases} \frac{(k^*)^{3/2}}{C_l y_d}, & \text{if } y < y_d, \\ \frac{(k^*)^{3/2}}{C_l y}, & \text{else}, \end{cases} \quad (28)$$

where $y_d = 2C_l\mu_l/(\rho\sqrt{k^*})$. Dependence (28) assumes a variation of ϵ in the viscous sublayer because $y_d \approx 0.5y_v$. This approach has been also used in the current research.

The wall function for the turbulent energy k is used in form (7), (8) and depends on the right-hand side $R_{hk}(y)$ represented by equality (20). It includes the dissipation ϵ and derivative $\mathrm{d}U/\mathrm{d}y$. The former term is taken from (28) while the last term is evaluated in the interval $[0, y^*]$ from the reduced momentum equations (13), (16):

$$(\mu_l + \mu_t)\mathrm{d}U/\mathrm{d}y = [(\mu_l + \mu_t^*)U(y^*) + f_2 R_{hu}]/f_1 + (y - y^*)R_{hu}, \quad (29)$$

where the turbulent viscosity μ_t is defined by (21). Eq. (29) is obtained by the integration of Eq. (12) and use relation (5) to exclude $\mathrm{d}U/\mathrm{d}y(y^*)$. Thus, this equation relies on the PNS assumptions used.

To evaluate y_v from (26), it is possible to use the value k^* instead of k_v. It allows us to simplify the evaluation algorithm for y_v substantially. First, a similar opportunity was noticed in [3]. Another way is based on computing k_v via k^* using (19), (20), (28) and (29). This approach is formally more precise on the one hand, and more complicated and less robust on the other hand. An additional analysis is required to evaluate its

utility in the trade-off between accuracy and robustness. The estimation of Re_v is varied between 10.8 and 20 [3,16]. It corresponds to the interval between the upper limit of the viscous sublayer and the point at which the linear and logarithmic parts of the velocity profile intersect for the channel flow [17]. It is not clear which value in this interval is most appropriate to approximation (21). In all computational results given below, $Re_v = 12$.

Thus, the coefficients f_1 and f_2 in wall functions (5)–(9) depend only on y^* and k^*. The latter value is determined from the solution of the HR model at the boundary point y^*. Hence, the intermediate boundary conditions (7) at $y = y^*$ complete the boundary-value problem in interval $[y^*, y_e]$ (y_e is the external boundary of the computational domain) and can be considered as generalized wall functions. These boundary conditions are of Robin-type and similar to the "slip boundary condition" at the edge of the Knudsen-layer in aerodynamics. It is important to note that the boundary conditions are linear with respect to the leading variable. As it follows from (5) and (7), the source terms in the wall functions can only be essential far enough from the wall because of the quadratic dependence of f_2 on y^*.

It worth noting that, although the problem is solved in the bulk domain $[y^*, y_e]$ only, the flux to the wall (e.g., skin friction) can be easily evaluated considering (10) (or its analogy for the temperature in the case of heat flux).

Upon obtaining a HR solution, it can be extended to interval $[y_v, y^*]$ using the analytical solution if $y_v \leqslant y^*$:

$$\begin{aligned} &u(y) = u(0) + \phi_1(y)u_y^* - \phi_2(y)\frac{R_h}{\mu^*},\\ &\phi_1 = \alpha_\mu y_v(1 + \theta \ln \Omega(y)),\\ &\phi_2 = \alpha_\mu y_v[y^* - \theta y + (\theta^2\alpha_\mu - 1/2 + \theta)y_v],\\ &\Omega = 1 + (\alpha_\mu - 1)\frac{y - y_v}{y^* - y_v}. \end{aligned} \tag{30}$$

It means that the intermediate boundary is not necessarily to be related to the nearest to the wall cell. It is possible to take y^* far enough from the wall and complement the solution on the region of the sublayer by (30).

If a heat transfer problem is considered, where buoyancy force is important, it is not difficult to take into account the appropriate term $\beta(T(y))$ in R_{hu}. In this case, the analytical solution (30) for the temperature (if $y_v \leqslant y \leqslant y^*$) is substituted to the right-hand side R_{hu} for the momentum equation. Since R_{hu} is variable, the wall functions for the velocity are used in form (7), (8). If y^* is in the sublayer, then β can be sufficiently evaluated by the value $\beta(T_w)$. Also, dependence $\mu_l = \mu_l(T)$ can be taken into account using either linear or quadratic approximation, as in [3], and easily implemented.

The generalized wall functions obtained and their implementations are not based on a numerical integration in the inner region $[0, y^*]$, as in [1–3], therefore the location of the intermediate boundary is not very substantial for the mesh distribution in the bulk domain. It means we can choose, e.g., a fine mesh despite a relatively big value of y^* (or vice versa) without loose of stability.

4. Numerical solution

In numerical simulation of turbulence, the numerical schemes, which preserve positiveness of a solution [15], are very efficient because unknown variables such as the turbulent kinetic energy k or its dissipation ϵ must be positive. The following numerical procedure is suggested for using the positive definite schemes in solving boundary-value problems with Robin-type boundary conditions.

Boundary condition (7) can be rewritten in the following general form:

$$k(0) = \alpha \mathrm{d}k/\mathrm{d}y(0) + \beta, \tag{31}$$

assuming that both the function k and its derivative $\mathrm{d}k/\mathrm{d}y$ are positive. This assumption is valid in the case of real physical problems for the turbulent kinetic energy in the wall vicinity. The coefficient α is positive because f_1 is always positive but the coefficient β can be negative (mostly, where $\epsilon > P_k$). In computations it can lead to a negative value of k. To avoid such a case, it is suggested to rewrite (31) in the following form if $\beta < 0$:

$$k(0) = \alpha \mathrm{d}k/\mathrm{d}y(0) + \beta\frac{k(0)}{k^-(0)}$$

or

$$k(0) = \tilde{\alpha} \mathrm{d}k/\mathrm{d}y(0), \tag{32}$$

where $\tilde{\alpha} = \frac{\alpha}{1-\beta/k^-(0)}$ and $k^-(0)$ is the value of $k(0)$ taken from the previous either time step or iteration.

For stability, near the points, where β changes its sign, a relaxation procedure for the coefficients α and β can be used.

5. Decomposition method

In this section a decomposition method for solving equations in the LR models is derived. The main idea is given below for an arbitrary linear differential equation.

First, let us consider a linear Dirichlet problem in the interval $[0, y_e]$:

$$\begin{aligned} &Lu = f,\\ &u(0) = u_0, \quad u(y_e) = u_1. \end{aligned} \tag{33}$$

The entire computational domain $\Omega = [0, y_e]$ is decomposed by two sub-domains, an inner one $\Omega_1 = [0, y^*]$ and outer one $\Omega_2 = [y^*, y_e]$, where $y^* < y_e$.

Near the wall (in inner domain Ω_1), the following two boundary-value problems are solved:

$$Lu_1 = f, \quad u_1(0) = u_0, \quad \mathrm{d}u_1/\mathrm{d}(y)(y^*) = 0, \quad 0 \leqslant y \leqslant y^*, \tag{34}$$

$$Lu_2 = 0, \quad u_2(0) = 0, \quad \mathrm{d}u_2/\mathrm{d}(y)(y^*) = 1, \quad 0 \leqslant y \leqslant y^*. \tag{35}$$

It is easy to prove that the general solution to (33) on the inner domain Ω_1 is the following one:

$$u(y) = u_1(y) + \mathrm{d}u/\mathrm{d}y(y^*)u_2(y). \tag{36}$$

If we consider (36) at the point y^*, we have a Robin-type boundary condition for outer domain Ω_2:

$$u(y^*) = u_1(y^*) + \mathrm{d}u/\mathrm{d}y(y^*)u_2(y^*). \tag{37}$$

This boundary condition is exact if we set it at $y = y^*$. Thus, the boundary condition from the wall ($y = 0$) is transferred to the point y^*.

The problem on one domain Ω is split into two problems on domains Ω_1 and Ω_2. As a result, we have some version of a decomposition method.

In the case of Newman boundary conditions

$$\mathrm{d}u/\mathrm{d}y(0) = u(0), \quad u(y_e) = u_1, \tag{38}$$

the algorithm is similar to that for Dirichlet problem (33). Indeed, we solve the following two boundary-value problems:

$$Lu_1 = f, \quad \mathrm{d}u_1/\mathrm{d}y(0) = u_0, \quad u_1(y^*) = 0, \tag{39}$$

$$Lu_2 = 0, \quad \mathrm{d}u_2/\mathrm{d}y(0) = 0, \quad u_2(y^*) = 1. \tag{40}$$

The general solution to problem (38) on the inner domain Ω_1 is

$$u(y) = u_1(y) + u(y^*)u_2(y). \tag{41}$$

After derivation, a Robin-type boundary condition at y^* is obtained:

$$\mathrm{d}u/\mathrm{d}y(y^*) = \mathrm{d}u_1/\mathrm{d}y(y^*) + u(y^*)\mathrm{d}u_2/\mathrm{d}y(y^*). \tag{42}$$

After solution to problems (39) and (40), we use this boundary condition in outer domain Ω_2. In inner domain Ω_1, the solution to problem (38) is then obtained from (41), since $u(y^*)$ is known from the outer problem on Ω_2.

In the case of nonlinear equations, the decomposition procedure given above is used in nonlinear iterations.

Thus, the decomposition method described above allows us to split the problem into the two parts: the near-wall (including the viscous sublayer) problem and the outer one. At a first glance, we gain nothing obtaining three boundary-value problems instead of one. On the other hand, in the inner (near-wall) and outer domains the appropriate problems can be solved on different meshes using different approximations. The analysis of LR models shows that the behavior of the solution in the vicinity of the sublayer defers drastically from that in the rest bulk domain, therefore such a splitting can be useful. It is important to note that in uniform approaches (one domain only) the presence of two adjacent cells having substantially different sizes can lead to a loss of accuracy or even stability. Additionally, it is worth noting that the algorithms on solving the inner and outer problems can be easily parallelized.

Since functions $u_1(y)$ and $u_2(y)$ do not explicitly depend on the solution in the domain Ω_2 (the dependence is via the coefficients and right-hand side only), these functions can be calculated once and then used further along with the use of either HR or LR model in the external domain (similar to Ω_2). In this approach, the problem is only solved in the external domain, and the solution $v(y)$ is complemented on domain Ω_1 then by the following way:

$$v(y) = \alpha u_1(y) + u_y^* u_2(y), \tag{43}$$

where $\alpha = (u^* - u_2^* u_y^*)/u_1^*$, $u_y^* = \mathrm{d}u/\mathrm{d}y(y^*)$.

It is easy to verify that $v(y^*) = u^*$, $\mathrm{d}v/\mathrm{d}y(y^*) = u_y^*$. It guarantees a smooth junction of both the inner and outer solutions.

This method can be effective if similar boundary-value problems are considered. For instance, if an initial-boundary-value 2D problem is studied, we solve a boundary-value problem in one direction x and an initial problem in the other direction y. It is possible to calculate the "basis" functions u_1 and u_2 once at some point x_0 and use them for approximate complementing the solution further at the next points x_i.

The decomposition approach, as well as the wall functions developed, can be easily generalized and used for the problems with the variable viscosity and density.

6. Channel flow

A fully developed plane channel flow has been considered as a test case. The flow is simulated far enough from the edge of the channel, so that the problem is 1D [18]. The HR k–ϵ model has been used to test the wall function approach:

$$\begin{aligned}
&\frac{\partial}{\partial y}\left[(\nu + \nu_\mathrm{t})\frac{\partial U}{\partial y}\right] = p_x/\rho,\\
&\nu_\mathrm{t}\left(\frac{\partial U}{\partial y}\right)^2 - \epsilon + \frac{\partial}{\partial y}\left[(\nu + \nu_\mathrm{t}/Pr_k)\frac{\partial k}{\partial y}\right] = 0,\\
&C_{\epsilon 1}\frac{\epsilon}{k}\nu_\mathrm{t}\left(\frac{\partial U}{\partial y}\right)^2 - C_{\epsilon 2}\frac{\epsilon^2}{k} + \frac{\partial}{\partial y}\left[(\nu + \nu_\mathrm{t}/Pr_\epsilon)\frac{\partial \epsilon}{\partial y}\right] = 0,\\
&\nu_\mathrm{t} = C_\mu k^2/\epsilon, \quad C_{\epsilon 1} = 1.44, \quad C_{\epsilon 2} = 1.92,\\
&Pr_k = 1, \quad Pr_\epsilon = 1.3.
\end{aligned} \tag{44}$$

Here y is the distance to the wall, p_x is the pressure gradient in the channel which is assumed to be negative, and $\nu = \mu/\rho$.

In the computations given below the Reynolds number is defined as $Re_\tau = u_\tau h/\nu$, where $u_\tau = \sqrt{-hp_x/\rho}$ is the friction velocity, h is the half of the channel height. The dependence of the dimensionless velocity, $u^+ = U/u_\tau$, on the universal coordinate, $y^+ = yu_\tau/\nu$, is calculated using the approach described in this work and compared against the benchmark results.

As it follows from Section 3, the generalized wall functions have only one uncertain parameter which is the coordinate y^* of the point to which the boundary conditions are moved. In this work, calculations have been done for different values of y^* including those less than y_v (in the viscous sublayer).

It is not difficult to show that for this test case the accurate value of u_τ is reached for all Reynolds numbers if either a conservative scheme is used or the error of approximation vanishes. The generalized wall functions do not bring any additional error in the calculation of u_τ irrespectively of the value of y^*.

The velocity profiles u^+ obtained by the wall function approach are given below against $y^+ = yu_\tau/\nu$ for different values of y^*. The profiles are compared against the Reichardt's profile [19] representing the benchmark solution.

In Fig. 1 the velocity profile is given for $Re_\tau = 395$ and $y^{+*} = 1$; 50; 200. Although y^* is deeply in the viscous sublayer ($y^{+*} = 1$) the correspondence to the LR solution (Reichardt's profile) is quite well apart from the very small near-wall region. Even, if y^* is taken far from the viscous sublayer, the solution is quite close to the benchmark solution. In the last case ($y^* = 200$) a half

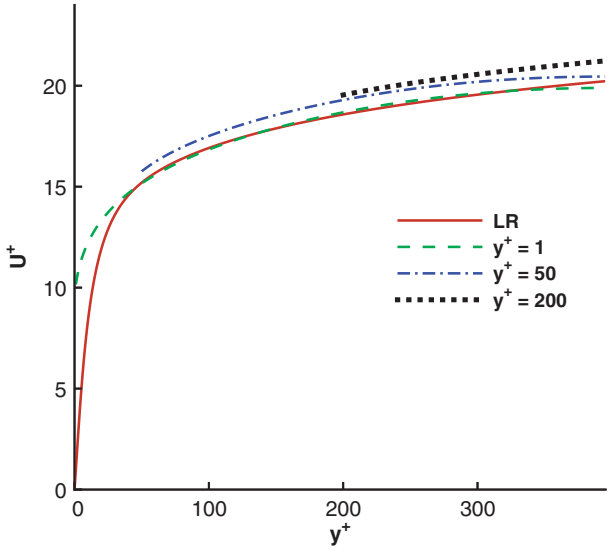

Fig. 1. Velocity profile in channel flow. $Re = 395$. Solid line is Reichardt's profile; the other lines correspond to $y^{+*} = 1$; 50; 200.

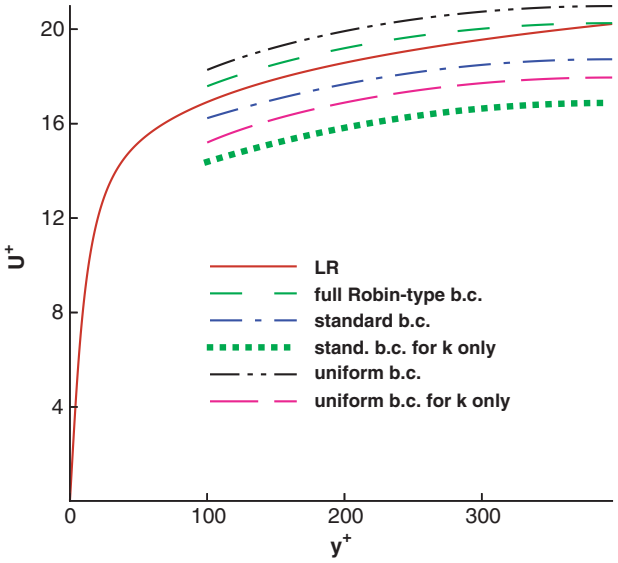

Fig. 2. Velocity profile in channel flow with different wall functions. Solid line is Reichardt's profile; the other lines correspond to: full boundary conditions (7) (dashed line); homogeneous Robin-type boundary conditions ($f_2 = 0$) for both U and k (dash-double-dot line) and only for k (long-dash line); "standard" wall function for all variables (dash-and-dot line) and only for k (dotted line).

of the domain is excluded in the case of the HR model; yet, in the bulk (rest) domain the solution is quite sensible. The calculations, here and in appropriate cases further, are done on a mesh chosen fine enough for the solution to be mesh independent on a graphic level.

A comparison between several different kinds of wall functions is shown in Fig. 2 for $y^{+*} = 100$. Full Robin-type boundary conditions (7) are represented by the dashed curve. The influence of the source term in (7) can be demonstrated by a comparison with homogeneous boundary conditions when the right-hand side is not taken into account ($f_2 = 0$). The neglect of the source terms for both the momentum and turbulent energy equations gives higher velocity (dash-double-dot curve). Meanwhile, neglecting only the source term in the turbulent energy equation leads to underestimation of the velocity (long-dash line). Replacement of boundary condition (7) for the turbulent kinetic energy k by the frequently used boundary condition $k^* = 1/3u_\tau^2$ gives a substantial deviation from the benchmark solution (dotted line). The standard wall functions used for all variables [18]

$$u^* = (1/\kappa \ln(u_\tau y^*/\nu) + 5)u_\tau, \quad k^* = 1/3u_\tau^2,$$
$$\epsilon^* = \kappa u_\tau^3/y^*, \quad \kappa = 0.41 \tag{45}$$

result in much better prediction (dash-and-dot line). Yet, it is worth noting that the channel flow is one of the most convenient test cases for the standard wall functions. The current approach gives more accurate prediction although the main advantages of the wall functions developed are expected at consideration of

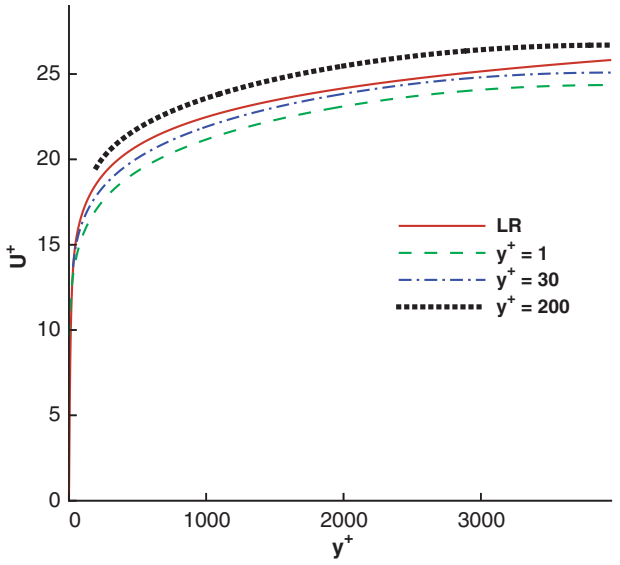

Fig. 3. Velocity profile in channel flow. $Re = 3950$. Solid line is Reichardt's profile; the other lines correspond to $y^{+*} = 1; 30; 200$.

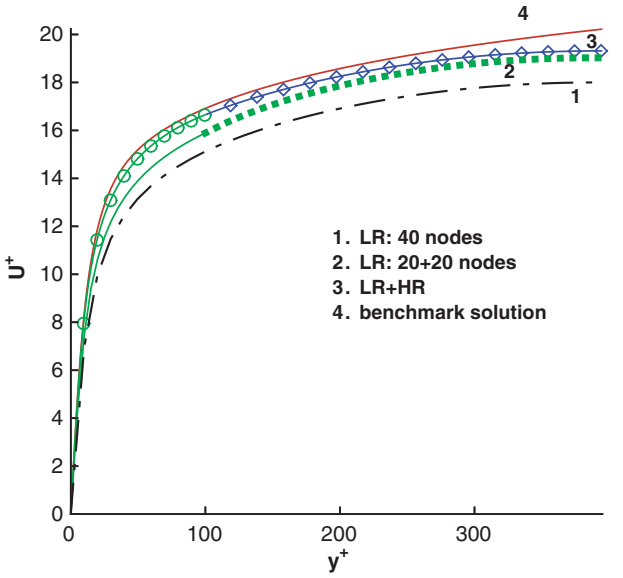

Fig. 4. Velocity profile in channel flow. Solid line is Reichardt's profile; dashed and dotted lines is solution of LR model by decomposition method with 20 and 20 points (each part); dashed-dotted line is 1-block solution with 40 points. Curve with circles and diamonds is composite LR and HR solution.

more complicated cases (see, e.g., the next test case on an impinging jet). It is important to emphasise that in contrast to the standard wall functions the approach in question is not based on the log-profile assumption for the velocity or any similar additional information to match the solution. Also, it is to be noted that the standard wall functions include the friction velocity u_τ, which is unknown in advance in a general case, that makes the boundary conditions nonlinear and demands appropriate iterations for resolving.

At higher Reynolds numbers, in general, the results are similar. In Fig. 3, the mean velocity profiles are shown for the case of $Re_\tau = 3950$ and $y^{+*} = 1;30;200$. The solution corresponding to $y^{+*} = 1$ almost coincides with the velocity profile obtained by standard wall functions (45).

The decomposition method described in Section 5 has been tested using the low-Reynolds number model by Chien [20]:

$$
\begin{aligned}
&\nu_t\left(\frac{\partial U}{\partial y}\right)^2 - \epsilon + \frac{\partial}{\partial y}\left[(\nu + \nu_t/Pr_k)\frac{\partial k}{\partial y}\right] = 0,\\
&C_{\epsilon 1} f_1 \frac{\widetilde{\epsilon}}{k}\nu_t\left(\frac{\partial U}{\partial y}\right)^2 - C_{\epsilon 2} f_2 \frac{\widetilde{\epsilon}^2}{k} + E + \frac{\partial}{\partial y}\left[(\nu + \nu_t/Pr_\epsilon)\frac{\partial \widetilde{\epsilon}}{\partial y}\right] = 0,\\
&\epsilon = \epsilon_0 + \widetilde{\epsilon}, \quad \nu_t = C_\mu f_\mu k^2/\epsilon, \quad f_\mu = 1 - \mathrm{e}^{-0.0115y^+},\\
&f_1 = 1, \quad f_2 = 1 - 0.22\mathrm{e}^{(-Re_T/6)^2}, \quad C_1 = 1.35, \quad C_2 = 1.8,\\
&\epsilon_0 = 2\nu\frac{k}{y^2}, \quad E = -2\nu\frac{\widetilde{\epsilon}}{y^2}\mathrm{e}^{-y^+/2}, \quad Re_t = \frac{k^2}{\widetilde{\epsilon}\nu}.
\end{aligned}
\tag{46}
$$

In Fig. 4 the dashed and dotted lines represent the solution obtained by the decomposition method with the junction point at $y^{+*} = 100$. In each sub-domain Ω_1 and Ω_2 the uniform mesh of 20 points is used. For comparison, the dash-dotted line corresponding to 1-block solution obtained on the uniform mesh of 40 points is given. The deviation from Reichardt's profile is explained by a very coarse mesh (in the case of a fine mesh the prediction is much more accurate). The calculation are advisedly done using the coarse mesh to show the capability of the decomposition method. In particularly, it is worth noting that the meshes used in the both domains have a substantially different size. The HR solution may be complemented on the whole domain using LR solution (43). It is shown by the curves with circles and diamonds. The complemented part of this solution on interval $[0\ y^{+*}]$ is given in Fig. 5 (dashed line). The curves marked by the squares and triangles represent the "basic" near-wall solutions u_1 and u_2 used in (43). The dotted line is analytical solution (30).

7. Impinging jet

Impinging jets are frequently used in many industrial applications where either heating or cooling processes are required. The heat transfer problem on a turbulent circular jet impinging onto a flat is well studied experimentally [5,21–23]. It became a test case for different turbulent models including the LR [6,25–29] and HR k–ϵ models [4,10,25,30].

The formulation of the problem is as follows. A fully turbulent air jet, generated in a pipelike nozzle, impinges on a flat surface at the right angle. The Reynolds num-

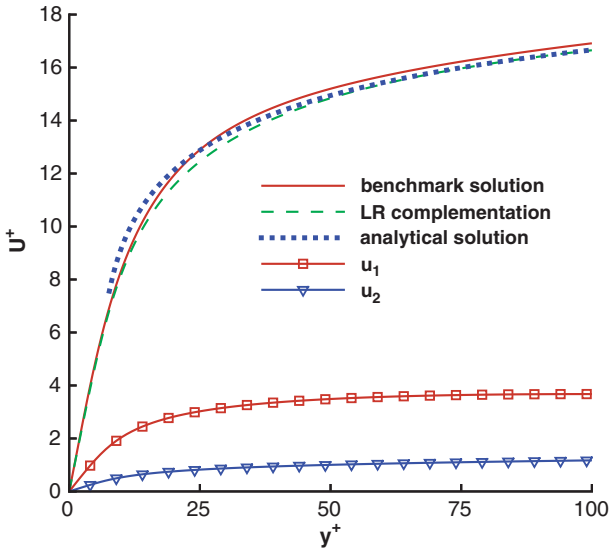

Fig. 5. Complemented velocity profiles. Solid line is Reichardt's profile; dashed is LR complementation (43); dotted line is analytical solution (30). Curves with squares and triangles are basic solutions u_1 and u_2 accordingly.

ber, based on the nozzle diameter $D = 0.0403$ m and the bulk velocity, is $Re = 23\,000$. The distance L between the nozzle and the surface equals to $2D$ and $6D$. Air is treated as an ideal gas and considered under normal conditions at temperature 293 K. The heated surface has constant temperature $T_w = 314.9$ K.

In the computations, the domain spans $13D$ in the radial direction. The grid includes 150×100 (axial $\times$ radial) nodes and 150×200 nodes. One should note here that for the validation purposes, preliminary comparisons of the results obtained on different meshes were done to check grid sensitivity. The boundary conditions at the edge of the nozzle are specified using the profiles for a fully developed turbulent pipe flow. The computations of the local Nusselt number are done for the different values of y^* or $Re_{y^*} \equiv \rho\sqrt{k^*}y^*/\mu_l$ calculated at the stagnation point.

The Nusselt number is defined as

$$Nu(r) = \frac{Dq(r)}{\kappa(T_w - T_b)}, \tag{47}$$

where r is the radial coordinate, $q(r)$ is the local heat flux, κ is the thermal conductivity coefficient, T_b is the bulk temperature of the jet.

It is well known that any linear eddy-viscosity model (EVM) drastically overpredicts the turbulent kinetic energy in the stagnation point region by an order of magnitude [30]. It inevitably leads to the considerable overestimation of the heat flux. So, the linear LR k–ϵ models give unacceptable overprediction by a factor of two, even more [2,27–29]. Furthermore, the linear k–ϵ model, as well as other EVM, is not entirely justified around the stagnation point because of the anisotropy of the flow. To improve prediction, along with the nonlinear EVM, some modifications of the EVM are used including the implementation of a realizability constraint [29], introduction of empirical formulas for the Prandtl number [27] and heat flux [10]. The application of the wall functions, in most cases, is also showed a poor performance [2,25,30]. More or less reasonable prediction was achieved in [2] using the Chieng and Launder wall function [31] and in [10] using the scalable wall functions. It is to be noted that in the latter case the empirical correlation was used for the local heat flux.

The HR k–ϵ model is employed in this investigation. No any empirical correlations are used.

The comparison of the local Nusselt number for $L = 2D$, calculated for $Re_{y^*} = 27$ and $Re_{y^*} = 320$, against experimental results [22,23] and computational results [24] based on the standard k–ϵ model is shown in Fig. 6. Although, the locations of y^*, to which the boundary conditions are transferred, are substantially different (an order of magnitude), the difference between the computational results mainly is a few percent. The standard k–ϵ model greatly overpredicts the local heat flux in the vicinity of the stagnation point.

The mean velocity profiles ($Re_{y^*} = 27$) are given in Fig. 7 at some locations downstream of the impinging jet. All the experimental data are represented by the appropriate diamond, gradient and square symbols; while the computational results are shown by the solid, dashed and dash-dot curves, accordingly at $r/D = 0.5$; 1; 2.5. At the region of the low mean velocity nearby the axis of symmetry ($r/D = 0.5$) and the region of acceleration of the flow ($r/D = 1$) the prediction of the velocity is quite reasonable. At $r/D = 2.5$, where the flow is decelerated, the prediction is not so good. At this location, substantial underprediction of the velocity in the near-wall region and overprediction in the outer region

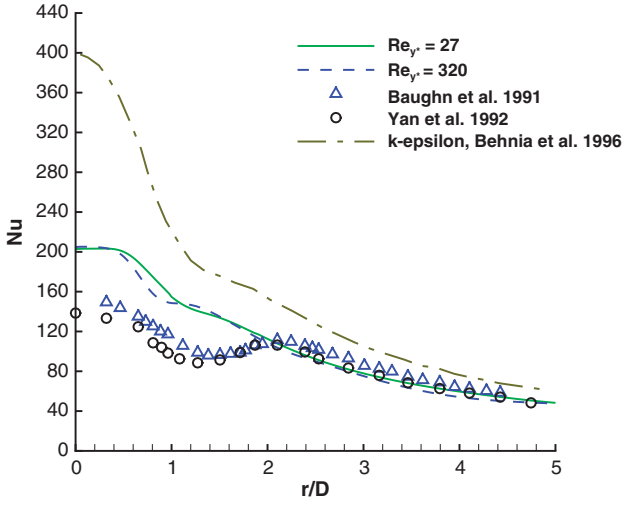

Fig. 6. Local Nusselt number for the impinging jet. Comparison of computational solutions for different y^* against experiments. $L/D = 2$.

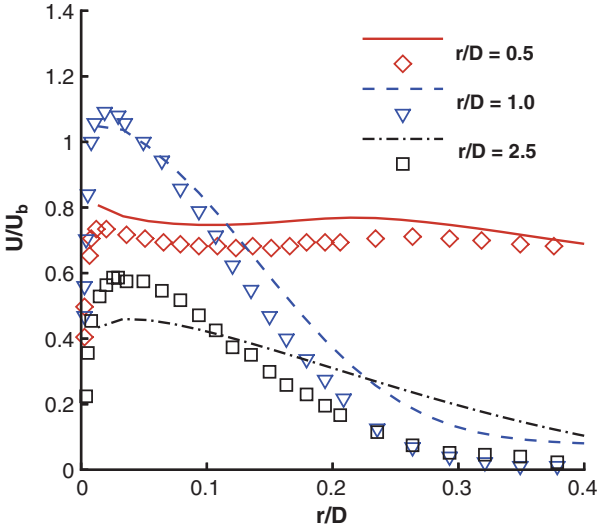

Fig. 7. Mean velocity in the impinging jet at $r/D = 0.5; 1; 2.5$.

were earlier noted for both the LR and HR linear k–ϵ models [6,10,28].

The comparison of the local Nusselt number for $L = 6D$ is shown in Fig. 8. The predicted results corresponding to $Re_{y^*} = 144$ and measured data [22,23] are presented here. In general, the conclusions are similar to the previous example. It worth noting that the standard k–ϵ model overpredicts the stagnation Nusselt number by about 120% [24].

The wall friction τ_w can be found similarly to the heat flux using formula (10). The distribution of the wall shear stress is represented in Fig. 9 for the case of $L/D = 2$ and $Re = 90\,000$. The prediction of the non-dimensional friction coefficient

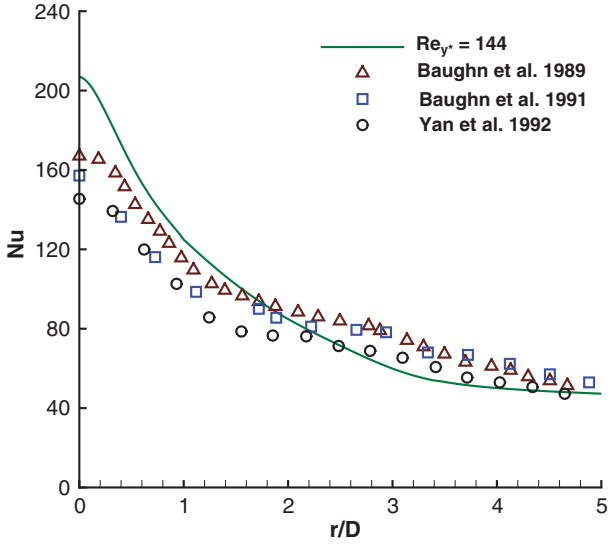

Fig. 8. Local Nusselt number for the impinging jet. Comparison of computational solutions against experiments. $L/D = 6$.

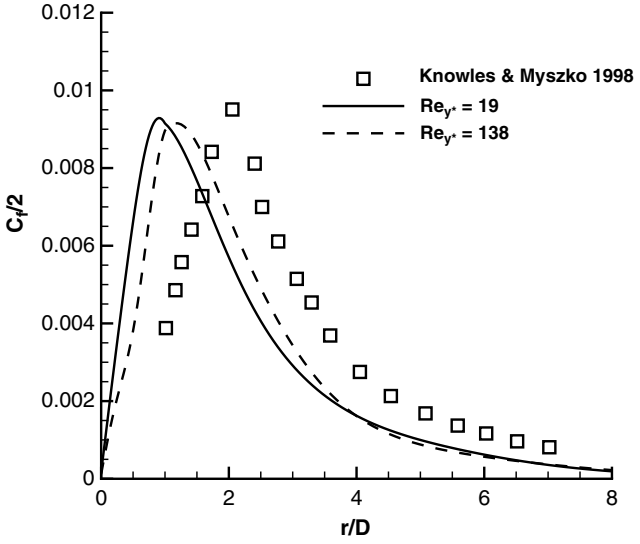

Fig. 9. Wall friction for the impinging jet. $L/D = 2$.

$$C_f = \frac{2\tau_w}{\rho U_b^2} \tag{48}$$

is given for $Re_{y^*} = 19$ and $Re_{y^*} = 138$. The curve marked by the squares represents the measurements of the maximal Reynolds shear stress divided by U_b^2. At the wall this value corresponds to $C_f/2$. The predicted function reaches almost the same value of the maximum but the peak is reached earlier. In general, the prediction is worse than for the heat flux.

8. Conclusion

The method of boundary condition transfer has been used to develop the generalized (Robin-type) wall functions for the HR turbulence models. They are based on the transfer of boundary conditions from a wall to some point in the computational domain (usually the nearest to the wall grid point). The boundary conditions at this point are of Robin-type and represented in a differential form. These boundary conditions are interpreted as the generalized wall functions taking into account source terms. The wall functions have been obtained in a compact easy-to-implement analytical form and they do not include any adjustable parameters. The mesh distribution inside the computational domain can be chosen independently of the location of the intermediate boundary. The implementation of this approach in the k–ϵ model shows the proposed wall functions to be quite accurate even if the boundary conditions are set at the point located either in a viscous sublayer or far beyond.

The generalized wall functions have been realized for the 1D test problem on fully turbulent channel flow and the 2D test case on the axisymmetrical impinging jet. Both heat flux and wall friction have been predicted.

The boundary condition for the normal velocity also is of Robin-type that means the normal velocity component does not necessarily equal zero. It allows one to be optimistic with respect to the possible application of the current approach to simulation of separated flows. This task will be studied in the future.

In application to the LR models, a decomposition method has been developed. It allows one to split the computational domain into a near-wall part and the rest one. The boundary-value problems in both parts can be solved independently using different numerical schemes and meshes.

Using the decomposition method, the HR solution can be complemented on the rest near-wall domain. This opportunity requires an additional investigation for multidimensional problems.

The wall functions and decomposition method can be easily generalized and used for the problems with variable viscosity and density.

A numerical robust approach, preserving positivity of a solution in the case of Robin-type boundary conditions, has been developed.

Acknowledgements

The author is grateful to A.V. Gerasimov and D.R. Laurence for fruitful discussions. This work has been partially supported by the FLOMANIA project (Flow Physics Modeling—An Integrated Approach) is a collaboration between Alenia, AEA, Bombardier, Dassault, EADS–CASA, EADS–Military Aircraft, EDF, NUMECA, DLR, FOI, IMFT, ONERA, Chalmers University, Imperial College, TU Berlin, UMIST and St. Petersburg State Technical University. The project is funded by the European Union and administrated by the CEC, Research Directorate-General, Growth Programme, under Contract No. G4RD–CT2001–00613.

The author thanks the anonymous referees for their useful remarks.

References

[1] Craft TJ, Gant SE, Gerasimov AV, Iacovides H, Launder BE. Wall-function strategies for use in turbulent flow CFD. In: Proceedings of 12th international heat transfer conference, Grenoble, France, 2002. p. 1–12.

[2] Craft TJ, Gant SE, Iacovides H, Launder BE. Development and application of a new wall function for complex turbulent flows. In: Proceedings of ECCOMAS CFD 2001 conference, Swansea, UK, 2001. p. 1–20.

[3] Craft TJ, Gerasimov AV, Iacovides H, Launder BE. Progress in the generalization of wall-functions treatments. Heat Fluid Flow 2002;23(2):148–60.

[4] Craft TJ, Gant SE, Iacovides H, Launder BE. A new wall function strategy for complex turbulent flows. Numer Heat Transfer 2004; 45:301–18.

[5] Cooper D, Jackson DC, Launder BE, Liao GX. Impinging jet studies for turbulence model assessment—I. Flow-field experiments. Int J Heat Mass Transfer 1993;36(10):2675–84.

[6] Craft TJ, Graham LJW, Launder BE. Impinging jet studies for turbulence model assessment—II. An examination of four turbulence models. Int J Heat Mass Transfer 1993;36(10): 2685–97.

[7] Patankar SV, Spalding DB. Heat and mass transfer in boundary layers. London: Morgan-Grampian Press; 1967.

[8] Launder BE, Spalding BI. The numerical computation of turbulent flows. Comput Methods Appl Mech Eng 1974;3:269–89.

[9] Grotjans H, Menter FR. Wall functions for industrial applications. In: Papailiou KD, editor. Proceedings of computational fluid dynamics'98, ECCOMAS, 1(2). Chichester, UK: John Wiley & Sons; 1998. p. 1112–7.

[10] Esch T, Menter FR. Heat transfer predictions based on two-equation turbulence models with advanced wall treatment. In: Proceedings of the 4th international symposium on turbulence, heat & mass transfer, Antalya, Turkey, 2003. p. 614–21.

[11] Wilcox DC. Wall matching, a rational alternative to wall functions. AIAA Paper 89-611, Reno, NV, 1989.

[12] Utyuzhnikov SV. Some new approaches to building and implementation of wall-functions for modeling of near-wall turbulent flows. Comput Fluids 2005;34(7):771–84.

[13] Drikakis D. Advances in turbulent flow computations using high-resolution methods. Prog Aerospace Sci 2003;39:405–24.

[14] Rubin SG, Tannehill JC. Parabolized/reduced Navier–Stokes computational techniques. Annu Rev Fluid Mech 1992;24:117–44.

[15] Lanerolle LWL. Positivity preserving pointwise implicit schemes with application to turbulent compressible flat plate flow. Int J Numer Methods Fluids 2001;35:903–38.

[16] Bredberg J, Peng S-H, Davidson L. On the wall boundary conditions for computing turbulent heat transfer with K–ω models. In: Kim JH, editor. Proceedings of the ASME heat transfer division, 5–10 November 2000, Orlando, USA, vol. 5. p. 243–50.

[17] Moser R, Kim J, Mansour N. Direct numerical simulation of the turbulent channel flow up to $Re = 590$. J Phys Fluids 1999;11: 943–5.

[18] Wilcox DC. Turbulence modeling for CFD. 2nd ed. Canada: DCW Industries; 2000.

[19] Hinze JO. Turbulence. 2nd ed. New York: McGraw-Hill; 1975.

[20] Chien K-Y. Predictions of channel and boundary-layer flows with a low-Reynolds-number turbulent model. AIAA 1982;20(1):33–8.

[21] Baughn J, Shimizu S. Heat transfer measurements from a surface with uniform heat flux and an impinging jet. Heat Transfer 1989;111:1096–8.

[22] Baughn J, Hechanova A, Yan X. An experimental study of entrainment effects on the heat transfer from a flat surface to a heated circular impinging jet. Heat Transfer 1991;111:1023–5.

[23] Yan X, Baughn JW, Mesbah M. The effects of Reynolds number on the heat transfer distribution from a flat plate to an impinging jet. ASME HTD 1992;226:1–7.

[24] Behnia M, Parneix S, Durbin PA. Accurate modeling of impinging jet heat transfer. In: Annual research briefs. Center for Turbulence Research, NASA Ames/Stanford University, 1997. p. 149–64.

[25] Heyerichs K, Pollard A. Heat transfer in separated and impinging turbulent flows. Int J Heat Mass Transfer 1996;39(12): 2385–400.

[26] Craft TJ, Iacovides H, Yoon JH. Progress in the of the non-linear two-equation models in the computation of convective heat transfer in impinging and separated flows. Flow Turbul Combust 1999;63:59–80.

[27] Park TS, Sung HJ. Development of a near-wall turbulence model and application to jet impingement heat transfer. Int J Heat Fluid Flow 2001;22:10–8.

[28] Merci B, Dick E. Predictive capabilities of an improved cubic k–ϵ model for inert steady flows. Flow Turbul Combust 2002;68: 335–58.
[29] Sunden B, Jia R, Abdon A. Computation of combined turbulent convective and impingement heat transfer. Int J Heat Fluid Flow 2004;14(1):116–33.
[30] Ashforth-Frost A, Jambunathan K. Numerical prediction of semi-confined jet impingement and comparison with experimental data. Int J Numer Methods Fluids 1996;23:295–306.
[31] Chieng CC, Launder BE. On the calculation of turbulent heat transport downstream from an abrupt pipe expansion. Numer Heat Transfer 1980;3:189–207.